Geoscience Frontiers 10 (2019) 107–117

HOSTED BY

ELSEVIER

Contents lists available at ScienceDirect

China University of Geosciences (Beijing)

Geoscience Frontiers

journal homepage: www.elsevier.com/locate/gsf

Research Paper

Source and possible tectonic driver for Jurassic–Cretaceous gold deposits in the West Qinling Orogen, China

Yafei Wu [a,b,c,*], Jianwei Li [a,c], Katy Evans [b], Denis Fougerouse [b], Kirsten Rempel [b]

[a] State Key Laboratory of Geological Processes and Mineral Resources, China University of Geosciences, Wuhan 430074, China
[b] School of Earth and Planetary Sciences, The Institute for Geoscience Research (TIGeR), Curtin University, GPO Box U1987, Perth, WA 6845, Australia
[c] School of Earth Resources, China University of Geosciences, Wuhan 430074, China

ARTICLE INFO

Article history:
Received 28 January 2018
Received in revised form
22 August 2018
Accepted 7 September 2018
Available online 9 October 2018

Keywords:
Pyrite LA-ICP-MS
Sulfur isotopes
Daqiao gold deposit
West Qinling Orogen
Paleo-Pacific plate
Jurassic–Cretaceous

ABSTRACT

The West Qinling Orogen (WQO) in Central China Orogenic Belt contains numerous metasedimentary rock-hosted gold deposits (>2000 t Au), which mainly formed during two pulses: one previously recognized in the Late Triassic to Early Jurassic (T3–J1) and one only recently identified in the Late Jurassic to Early Cretaceous (J3–K1). Few studies have focused on the origin and geotectonic setting of the J3–K1 gold deposits.

Textural relationships, LA-ICP-MS trace element and sulfur isotope compositions of pyrites in hydrothermally altered T3 dykes within the J3–K1 Daqiao deposit were used to constrain relative timing relationships between mineralization and pyrite growth in the dykes, and to characterize the source of ore fluid. These results are integrated with an overview of the regional geodynamic setting, to advance understanding of the tectonic driver for J3–K1 hydrothermal gold systems. Pyrite in breccia- and dyke-hosted gold ores at Daqiao have similar chemical and isotopic compositions and are considered to be representative of J3–K1 gold deposits in WQO. Co/Ni and sulfur isotope ratios suggest that ore fluids were derived from underlying Paleozoic Ni- and Se-rich carbonaceous sedimentary rocks. The geochemical data do not support the involvement of magmatic fluids. However, in the EQO (East Qinling Orogen), J3–K1 deposits are genetically related to magmatism. Gold mineralization in WQO is contemporaneous with magmatic deposits in the EQO and both are mainly controlled by NE- and EW-trending structures produced by changes in plate motion of the Paleo-Pacific plate as it was subducted beneath the Eurasian continent. We therefore infer that the J3–K1 structural regime facilitated the ascent of magma in the EQO and metamorphic fluids in the WQO with consequent differences in the character of contemporaneous ore deposits. If this is correct, then the far-field effects of subduction along the eastern margin of NE Asia extended 1000's of km into the continental interior.

1. Introduction

The far-field effects of changes in plate motion during Mesozoic subduction of the Paleo-Pacific plate have been invoked to explain changes in stress regime and widespread gold mineralization in NE Asia (Fig. 1; e.g., Zhai and Deng, 1996; Goldfarb et al., 1998, 2007; Qiu et al., 2002; Ratschbacher et al., 2003; Mao et al., 2005, 2006, 2008, 2010; Sun et al., 2007, 2010, 2013; Lan et al., 2011). However, the timing and reach of these far-field effects and their relation to gold mineralization at different distances from the plate boundary remain poorly understood. A better understanding of the geotectonic evolution of NE Asian response to such changes and their control on gold endowment is needed to design effective mineral exploration strategies.

The 2500 km long Qinling Orogenic Belt (QOB) in central China is an ideal place to determine how changes in plate motion affected the geodynamics and gold mineralization in the continental interior (Figs. 1 and 2). In the East Qinling Orogen (EQO), magmatism and genetically related Au, Cu-Mo and Pb-Zn deposits of Late Jurassic to Early Cretaceous age (J3–K1, ca. 150–125 Ma) are widely distributed (Fig. 2; e.g., Shanzha and Xiaoqinling; Mao et al., 2008,

* Corresponding author. State Key Laboratory of Geological Processes and Mineral Resources, China University of Geosciences, Wuhan 430074, China. Fax: +86 27 67885096.
E-mail address: yafei.wu@postgrad.curtin.edu.au (Y. Wu).
Peer-review under responsibility of China University of Geosciences (Beijing).

https://doi.org/10.1016/j.gsf.2018.09.005
1674-9871/

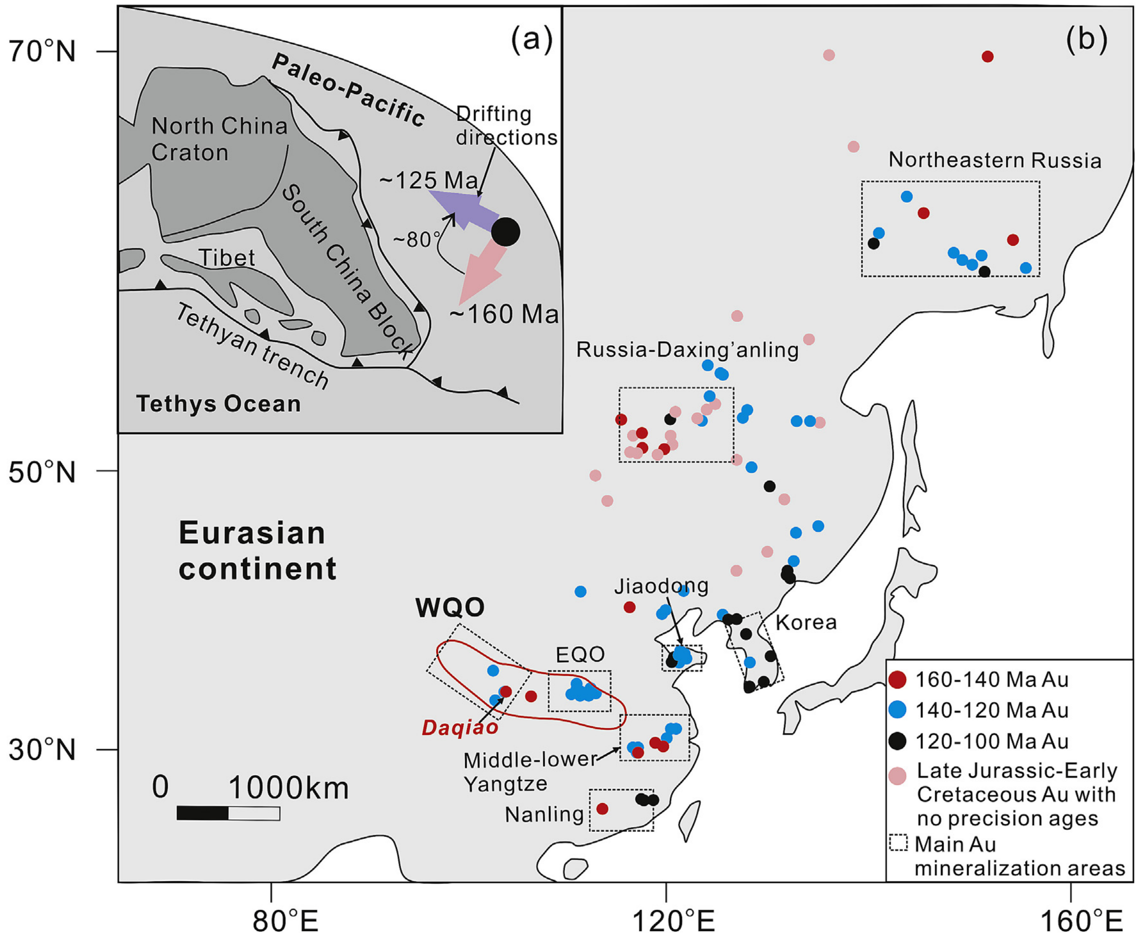

Figure 1. (a) Subduction and drifting history of the Paleo-Pacific plate since the Late Jurassic. (b) Main areas with intensive Late Jurassic to Early Cretaceous magmatism and related gold mineralization in the NE Asia. Modified after Sun et al. (2007), Mao et al. (2005) and Goldfarb et al. (2014).

2010; Li et al., 2012a, b; Xie et al., 2017). It has been suggested that tectonism during this period was affected by subduction of the Paleo-Pacific plate (Mao et al., 2008, 2010). In the West Qinling Orogen (WQO), most gold deposits are Late Triassic to Early Jurassic in age (T3–J1; ca. 216–203 Ma; Zeng et al., 2012; Liu et al., 2014; Wang et al., 2014; Hu, 2015; Zhang, 2016; Lin et al., 2017), and are spatially associated with intrusions and dykes (ca. 220–200 Ma; Dong et al., 2011; Dong and Santosh, 2016). However, a small number of Late Jurassic to Early Cretaceous (J3–K1) gold deposits in the WQO are not associated with magmatic activity (ca. 151–125 Ma; Huang et al., 1996; Lu et al., 2006; Qi et al., 2006; Liu et al., 2015b; Wu et al., 2018a, b). The formation of J3–K1 gold deposits without magmatism in the WQO, while Au, Cu-Mo, Pb-Zn deposits formed in response to magmatism in the EQO requires explanation.

The large Daqiao gold deposit (>105 t Au at 3–4 g/t) was studied to advance understanding of ore-formation in the WQO (Fig. 2). A detailed interpretation on sulfide generations hosted in breccia ores and their compositional and isotopic features areab provided in Wu et al., (2018a). High-precision sericite $^{40}Ar/^{39}Ar$ dates show that this J3–K1 deposit was produced by multiple episodes of hydrothermal activity between 151 Ma and 127 Ma (Wu et al., 2018b). Gold ore is hosted in Triassic turbidites and in granodiorite and diorite porphyry dykes dated at ca. 215–212 Ma and 188 Ma, respectively (Wu et al., 2018b). In this paper, the additional textures, chemical, and sulfur isotope compositions of the dyke-hosted pyrites are used to compare and further constrain the source of sulfur and ore fluids in the WQO. The J3–K1 deposits and setting in the WQO are then compared to those in the EQO.

2. Regional geological setting

Mesozoic oblique subduction of the Paleo-Pacific ocean plate beneath the Eurasian continent is thought to have started at ca. 160 Ma (Fig. 1a; Ren et al., 1992; Niu et al., 2003). The drifting direction of the Paleo-Pacific plate changed from roughly SW at ca. 160 Ma to NW at ca. 125–122 Ma (Koppers et al., 2003; Sun et al., 2007). At ca. 160 Ma, the principal stress direction in the QOB was NS and gradually shifted to EW by ca. 140 Ma (Mao et al., 2005, 2006). Polymetallic deposits genetically associated with the subduction-related magmatic centers occur across the whole NE Asia with peaks at ca. 150–140 Ma and 130–119 Ma (Fig. 1b; Mao et al., 2005, 2008; Li et al., 2003, 2006, 2012a, b; Goldfarb et al., 2014).

The QOB is separated from the North China Craton (NCC) by the Luonan-Luanchuan Fault and from the South China Block (SCB) by the Triassic Mianlue suture zone (Fig. 2; Zhang et al., 2001; Dong et al., 2011, 2013). This orogen records subduction of proto-Tethyan oceanic crust collision between the NCC and Qinling micro-plate along the Shangdan suture in the Middle Paleozoic, and subduction of the paleo-Tethyan oceanic crust and collision between the Qinling terrain and the SCB along Mianlue suture in the

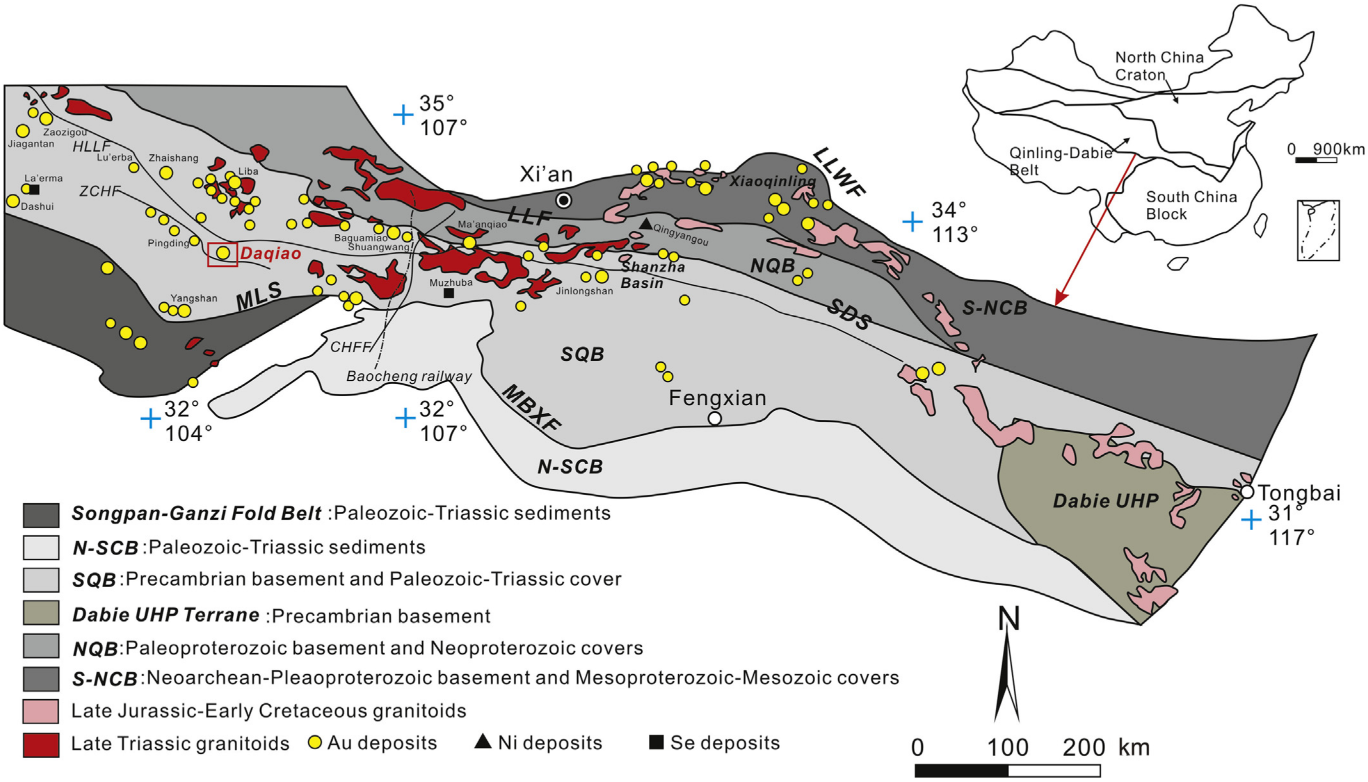

Figure 2. Simplified geologic map showing tectonic division of the Qinling Orogenic Belt (modified after Dong and Santosh, 2016). Also shown are the distribution of major faults, granitoid intrusions, and gold deposits, such as Daqiao. The insert shows the location of the Qinling Orogen in China. LLWF: Lingbao-Lushan-Wushan Fault; LLF: Luonan-Luanchuan Fault; SDS: Shangdan Suture; HLLF: Hezuo-Lintan-Liangdang Fault; ZCHF: Zhouqu-Chengxian-Huixian Fault; CHFF: Chengxian-Huixian-Fengxian Fault; MLS: Mianlue Suture; MBXF: Mianlue-Bashan-Xiangguang Fault; S-NCC: Southern North China Craton; NQB: North Qinling Belt; SQB: South Qinling Belt; N-SCB: Northern South China Block; Dabie UHP: Dabie Ultrahigh Pressure Terrane.

Early Mesozoic (Meng and Zhang, 1999; Dong et al., 2011). The QOB can be divided into four suture zone or thrust fault bounded terranes from north to south (Fig. 2): the Southern North China Craton (S-NCC), North Qinling Belt (NQB), South Qinling Belt (SQB) and Northern South China Block (N-SCB) (Zhang et al., 1995). The QOB has also been divided into the eastern and western parts (EQO and WQO). Both are dominated by the Cambrian to Triassic marine sedimentary rocks, with some Archean metamorphosed supracrustal rocks in the EQO (Li et al., 2012a; Liu et al., 2015a).

Mesozoic granitoid intrusions are widespread in the QOB (Fig. 2; Dong and Santosh, 2016). The majority of intrusions in the WQO (ca. 230–200 Ma) contain mafic enclaves and are enriched in LILE with negative $\varepsilon_{Nd}(t)$ and $\varepsilon_{Hf}(t)$ values. J3–K1 (164–100 Ma) intrusions are rare in the WQO but are widespread in the EQO (Fig. 2). J3–K1 granitoids commonly contain biotite and hornblende, have high Mg# and higher $\varepsilon_{Hf}(t)$ values than Late Triassic granitoids, which indicate they assimilated less continental crust (Wu et al., 2014).

3. Deposit geology

The Daqiao gold deposit is located between the northern Hezuo-Lintan-Liangdang Fault (HLLF) and the southern Zhouqu-Chengxian-Huixian Fault (ZCHF; Fig. 2; Zhang et al., 2018). Gold mineralization is mainly hosted in Middle Triassic Huashiguan Formation turbidites that are in fault contact with Carboniferous limestone (Zhang et al., 2018; Wu et al., 2018a). There are a number of reverse faults in the mine, which mostly strike NE. Ore bodies at Daqiao are characterized by auriferous breccias (Fig. 3a) and are spatially related to the NE-striking reverse faults. Hydrothermal alteration consists of multistage silicification, sulfidation, sericitization and carbonatization (Fig. 3b). Arsenian pyrite and marcasite are the predominant ore minerals (Wu et al., 2018a).

A number of granodiorite dykes and a few diorite porphyry dykes intrude the Triassic sediments at Daqiao (Fig. 3c and d). Individual dykes extend for several tens to a few hundred meters along northeast or northwest strike and are 2–10 m in thickness. In gold ore bodies, these dykes exhibit variable degrees of silicification, sericitization, sulfidation, carbonatization, and gold mineralization (Fig. 3c–f). Recent LA-ICP-MS zircon U–Pb dating of the granodiorite and diorite porphyry dykes suggests they were emplaced at ca. 215–212 Ma and 188 Ma, respectively (Wu et al., 2018b).

Two kinds of pyrite have been identified in granodiorite dykes with different degrees of hydrothermal alteration (Fig. 3c–f). In the less intensely altered dykes (Fig. 3c, e), pyrite occurs as fine-grained anhedra to subhedra (20–100 μm across), or in deformed and cataclastic aggregates (150–600 μm across). Pyrite commonly contains inclusions of, or occurs as veinlets with, chalcopyrite, galena, and sphalerite. Irregular and deformed pyrite aggregates replace silicate minerals (Fig. 3e). In dykes with intense alteration, pyrite is subhedral, between 200 and 300 μm in diameter (Fig. 3d, f), has a characteristic porous texture, and contains fine-grained inclusions of mica and feldspar (2–20 μm across).

4. Samples and methods

4.1. Sample description

Polished thin sections and section blocks of dykes containing pyrite were characterized initially by optical microscopy and

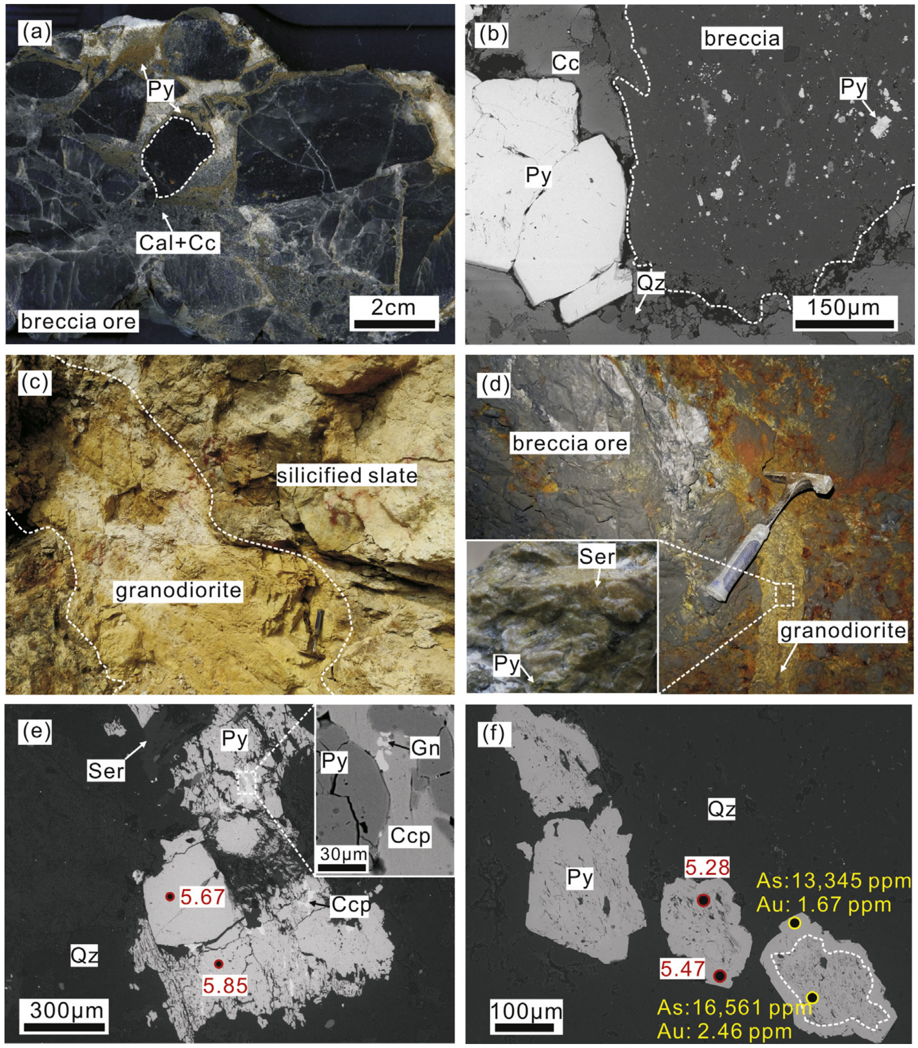

Figure 3. Photographs (a, c, d) and back-scattered electron (BSE) images (b, e, f) showing the features of gold mineralization, altered dykes and disseminated pyrite at Daqiao. (a) Black silicified siltstone was cemented by the calcite-chalcedony-pyrite matrix forming high-grade breccia ore. (b) Silicified breccia with disseminated sulfides is surrounded by later calcite-quartz-pyrite. (c) Granodiorite dyke intruding slates of the Triassic Huashiguan Formation. (d) Contact between breccia ore and intensely altered granodiorite dykes with aggregates of sericite and pyrite (the inset). (e) Deformed and cataclastic pyrite subhedras and pyrite aggregates intergrown with chalcopyrite, sphalerite, galena, and sericite. Smooth and porous pyrites have similar sulfur isotope compositions. (f) Subhedral pyrite grains with porous cores containing fine-grained silicate inclusions. The rim and core have high Au-As concentrations and similar sulfur isotope compositions. Cal: Chalcedony, Cc: calcite, Ccp: chalcopyrite, Gn: galena, Py: pyrite, Qz: quartz, Ser: sericite, Sp: sphalerite.

scanning electron microscopy (SEM). Two samples of altered and mineralized granodiorite dykes (DQ123 with 0.4 g/t Au, and DQ477 with 2.5 g/t Au) were collected from borehole ZK6802 and underground workings, respectively, that are 2.5 km apart. Sample DQ123 is less intensely altered than DQ477, which contains coarse-grained sericite and pyrite aggregates (Fig. 3d).

4.2. LA-ICP-MS multi-element analysis of sulfides

The trace element concentrations of pyrite in each granodiorite dyke samples were determined by laser ablation inductively coupled plasma mass spectrometry (LA-ICP-MS). The analytical instrumentation employed in this study was a Photon Machines Analyte G2 LA system (193 nm, 4 ns excimer laser) attached to a PerkinElmer DRC-e ICP-MS, at the U.S. Geological Survey, Denver Federal Center. Laser ablation was carried out using a 30 μm spot size, a fluence of 5 J/cm^2 at 7 Hz with a 35 s baseline and 40–50 s of ablation. Ablated materials were transported in He carrier gas to a modified glass mixing bulb where the He and sample aerosol were mixed coaxially with Ar prior to the ICP torch. Concentration and detection limit calculations were conducted using the protocol of Longerich et al. (1996). Signals were calibrated using USGS MASS-1 sulfide reference material and iron (^{57}Fe) was used as the internal standard (Wilson et al., 2002). The reference material (MASS-1) was analyzed 5–10 times at the beginning of the analytical session and monitored throughout the session for drift. Signals were screened visually for heterogeneities such as micro-inclusions or zoning. The results are given in Table 1, and the reported mean concentrations for trace elements were calculated assuming that concentrations are zero for spot analyses below detection limit (b.d.l.).

4.3. LA-MC-ICP-MS sulfur isotope analysis

Polished thin sections and section blocks analyzed using LA-ICP-MS trace element spot analysis were re-polished and used for in-situ sulfur isotope analysis. In situ S isotope analyses of pyrite were performed using a Nu Plasma HR multicollector ICP-MS together with a Photon Machine Analyte G2 laser system, at the Geological Survey of Finland (GSF), Espoo, Finland. Samples were

Table 1
LA-ICP-MS trace element (in ppm) analysis of pyrite hosted by altered granodiorite dykes at the Daqiao gold deposit.

Analysis No.	Co	Ni	Cu	Zn	As	Se	Ag	Sn	Sb	Te	Au	Tl	Pb
DQ123-1	53.92	120	0.18	0.68	483.6	77.13	0.01	0.01	0.01	1.02	0	0	0.01
DQ123-2	80.19	574.94	0.29	0.85	3875.84	47.61	0.31	0.05	6.67	0.26	0	0.02	0.01
DQ123-3	191.28	34.56	2.04	0.57	14377.83	57.9	0.04	0.01	1.33	1.07	2.63	0	5.45
DQ123-4	14.36	12.78	0.87	0.31	6279.39	45.75	0.21	0.03	1.73	0.94	0.9	0	4.01
DQ123-5	3.16	3.84	1.93	0.22	9816.91	51.09	0.08	0.02	0.37	3.41	3.28	0	0.54
Mean	68.58	149.22	1.06	0.53	6966.71	55.90	0.13	0.02	2.02	1.34	1.36	0.00	2.00
S.D.	67.27	216.79	0.79	0.23	4798.02	11.40	0.11	0.01	2.41	1.08	1.36	0.01	2.28
DQ477-1	0.91	23.86	98.45	1.27	22624.49	458.31	3.84	0.02	30.53	6.03	2.99	1.93	37.65
DQ477-2	160.49	649.19	98.77	1.23	13345.52	464.46	6.61	0.24	120.69	8.34	1.67	0.46	203.38
DQ477-3	3.37	123.42	88.52	1.9	16560.87	437.39	6.84	1.61	96.55	5.31	2.46	1.55	65.31
Mean	54.92	265.49	95.25	1.47	17510.29	453.39	5.76	0.62	82.59	6.56	2.37	1.31	102.11
S.D.	74.65	274.34	4.76	0.31	3847.15	11.59	1.36	0.70	38.11	1.29	0.54	0.62	72.49

S.D. = Standard deviation.

ablated in He gas (gas flows = 0.4 and 0.1 L/min) within a HelEx ablation cell (Müller et al., 2009). During ablation, the data were collected in static mode (^{32}S, ^{34}S). Pyrite was ablated using a spot size of 30 μm and a fluence of 0.83 J/cm^2 at 5 Hz. The total S signal obtained for pyrite was typically 1.0–1.2 V. Under these conditions, after a 20 s baseline, 50–60 s of ablation is needed to obtain an internal precision of $^{34}S/^{32}S \leq \pm$ 0.000005 (1 SE). Three pyrite standards were used for external standard bracketing (PPP-1) (Gilbert et al., 2014) and quality control (Pyrite1 and Pyrite2 from GSF) of analyses (Wong et al., 2017). The results are given in Table 2.

5. Results

Pyrite from the altered dykes at Daqiao contains many trace elements (Fig. 4; Co, Ni, Cu, Zn, As, Se, Ag, Sb, Te, Au, Tl, and Pb). The gold content of DQ123 pyrite grains varies from b.d.l to 3.28 ppm (mean = 1.36 ppm, standard deviation (s.d.) = 1.36, n = 5), while arsenic varies from 484 ppm to 14,378 ppm (mean = 6967 ppm, s.d. = 4798, n = 5). In DQ477, the gold concentration ranges from 1.67 ppm to 2.99 ppm (mean = 2.37, s.d. = 0.54, n = 3) and arsenic from 13,346 ppm to 22,624 ppm (mean = 17,510 ppm, s.d. = 3847, n = 3). Although pyrite spot analyses from the two dyke samples demonstrate similar trace element patterns, a number of trace elements are more enriched in sample DQ477 than DQ123 (Fig. 4e), for instance, Ni (mean 265.5 ppm vs. 149.2 ppm), Se (453.4 ppm vs. 55.9 ppm), Cu (95.2 ppm vs. 1.1 ppm), Ag (5.8 ppm vs. 0.1 ppm), Sb (82.6 ppm vs. 2.0 ppm), Te (6.6 ppm vs. 1.3 ppm), and Pb (102.1 ppm vs. 2.0 ppm).

The $\delta^{34}S$ signatures of fourteen spot analyses of pyrite from these two dyke samples range from +4.9‰ to +7.1‰ (Fig. 5; mean + 5.6‰, s.d. = 0.5). In DQ123, with the exception of one analysis at +7.1‰, all the pyrite grains show a relatively homogenous $\delta^{34}S$ values from +4.9‰ to +6.0‰ (mean = +5.8‰, s.d. = 0.6, n = 8). In DQ477, $\delta^{34}S$ values of all the pyrite grains have narrow range of $\delta^{34}S$ values from +5.3‰ to +6.0‰ (mean = +5.5‰, s.d. = 0.2, n = 6).

Table 2
LA-MC-ICP-MS in situ sulfur isotope composition of pyrite hosted by altered granodiorite dykes at the Daqiao gold deposit.

Analysis No.	Sulfide type	$\delta^{34}S$ (‰, VCDT)	2σ
DQ123-1	Pyrite	7.1	0.2
DQ123-2		5.7	0.2
DQ123-3		6.0	0.2
DQ123-4		5.9	0.3
DQ123-5		5.2	0.2
DQ123-6		5.7	0.3
DQ123-7		5.7	0.2
DQ123-8		4.9	0.2
Mean		5.8	0.2
S.D.		0.6	0.0
DQ477-1	Pyrite	5.3	0.2
DQ477-2		5.5	0.2
DQ477-3		5.3	0.2
DQ477-4		5.3	0.3
DQ477-5		6.0	0.2
DQ477-6		5.5	0.2
Mean		5.5	0.2
S.D.		0.2	0.0

S.D. = Standard deviation.

6. Discussion

Previous geochronological studies suggest that the majority of gold deposits and igneous intrusions in the WQO have T3–J1 ages (ca. 225–180 Ma) and formed in a syn- to post-collisional setting (Fig. 6; Dong et al., 2011). Only a few gold deposits of J3–K1 age have been reported (Wu et al., 2018b), and these show no association with magmatic activity in the WQO (Fig. 6). The substantial time gap between the youngest records of extensional deformation in the Qinling Orogen (e.g., the ca. 188 Ma dykes at Daqiao), the lack of J3–K1 magmatism, and the small number of J3–K1 gold deposits in the WQO suggests that the J3–K1 gold deposits are related to a poorly characterized geotectonic event.

If pyrite hosted in T3–J1 dykes at Daqiao records fluid flow associated with the J3–K1 mineralization events, then the trace element contents and sulfur isotope ratios of the pyrite can be used to characterize the fluid source, and, in conjunction with the regional geodynamic context, to draw conclusions on the time-scales and nature of the causes of the fluid flow.

6.1. Relationship of dyke-hosted pyrite to J3–K1 mineralization at Daqiao

Petrogenesis and Lu-Hf isotope studies suggest that pyrite-bearing granodiorite dykes at Daqiao are mainly produced by partial melting of thickened lower crust in a compressional setting (Shan et al., 2016). This is consistent with evidence from contemporaneous intrusions in the WQO (ca. 220–210 Ma), such as Al-saturation, LILE enrichment, negative $\varepsilon_{Nd}(t)$ and $\varepsilon_{Hf}(t)$ values (Sun et al., 2002; Zeng et al., 2014). Texturally, pyrite in the intensely altered dykes is similar to early-ore stage subhedral pyrite disseminations in the breccia-hosted ores at Daqiao (Wu et al., 2018a). However, the deformed and cataclastic pyrite aggregates in less intensely altered dykes are typically intergrown with other sulfide phases and are texturally dissimilar to pyrite in breccia-hosted ores.

The As and Au composition of pyrite from the two dykes (DQ123 and DQ477) are comparable (mean 6967 ppm vs. 17,510 ppm As;

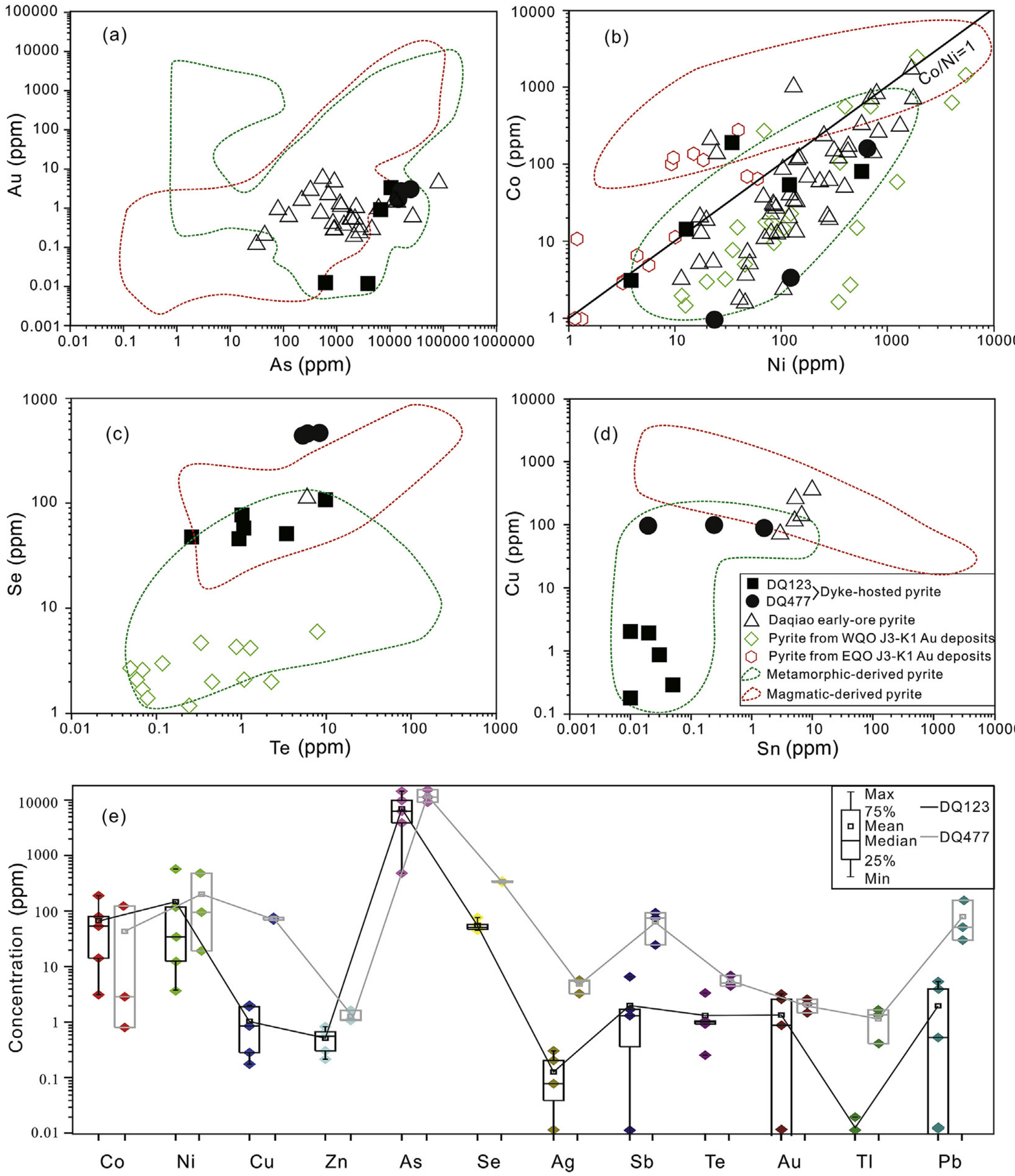

Figure 4. Plots of LA-ICP-MS spot analyses on pyrite compared with the compositional ranges of magmatic- and metamorphic-derived pyrite, using data from Belousov et al. (2016) and Keith et al. (2018), trace element contents of pyrite in Daqiao early-ore stage breccia-hosted ores (Wu et al., 2018a), and of pyrite from other gold deposits of J3–K1 ages in areas nearby WQO and EQO (Zhang et al., 2014; Bi et al., 2016). (a) As-Au: Most pyrites show high Au and As, falling into the metamorphic region. (b) Ni-Co: Most of pyrite from Daqiao deposit and gold deposits in WQO have Co/Ni in the metamorphic/sedimentary region. (c) Te-Se: Pyrite from DQ477 has higher Se content than pyrite from DQ123 and other gold deposits in WQO. (d) Sn-Cu: Pyrite from DQ477 and Daqiao early-ore stage have higher Cu contents than pyrite from DQ123, and most spot analyses plot in the metamorphic-derived pyrite region. (e) Comparison of pyrite trace element variation patterns between DQ123 and DQ477.

1.36 ppm vs. 2.37 ppm Au), and mostly plot within the range of Daqiao early-ore stage pyrite with up to 87,444 ppm As and 5.7 ppm Au (Fig. 4a). The lower abundance of trace elements (Fig. 4; Au, As, Se, Co, Te, Cu, and Sn) and less intense alteration in DQ123 (Fig. 3c) relative to DQ477 may be indicative of a fluid flow of lower temperatures and/or fluid-rock ratios than DQ477. However, the lower abundance of trace elements in DQ123 pyrite could also be due to sequestration of these elements in other sulfides (Fig. 3e; e.g., Co and Se into sphalerite, Se into chalcopyrite; Large et al., 2009; Genna and Gaboury, 2015). The δ^{34}S values of dyke-hosted pyrite, which range from +4.9‰ to +7.1‰ (mean + 5.6‰) is similar to that of the early-ore stage pyrite (mean + 4.4‰; Wu et al., 2018a). Together, the trace element, and sulfur isotopic characteristics of early-ore stage breccia-hosted and dyke-hosted pyrite are representative of the J3–K1 fluids that formed Daqiao gold mineralization. However, the J3–K1 fluid flow may have been episodic and cyclic, which is consistent with the complex breccia ores in the mine.

6.2. Characteristics of J3–K1 fluid flow in the dykes at Daqiao

Pyrite trace elements compositions (e.g., Co, Ni, and Se) have commonly been used to assess origin (e.g., Price, 1972; Huston et al., 1995; Belousov et al., 2016). For example, pyrite from volcanic exhalative and felsic intrusion-related sulfide ores generally has hundreds of ppm Co, tens of ppm of Ni with Co/Ni = 5–50 (Price, 1972). Elevated Co/Ni is caused by the more rapid extraction of Ni

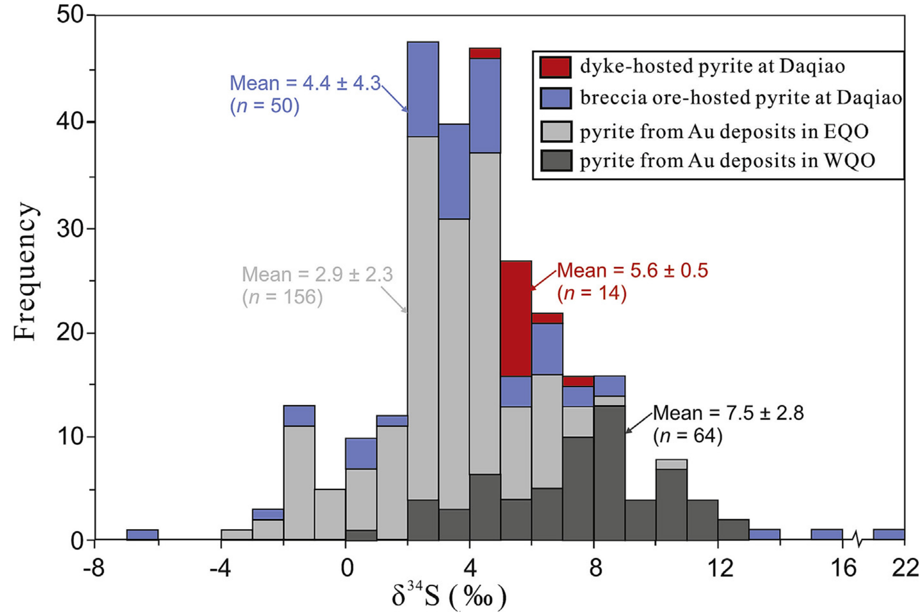

Figure 5. Sulfur isotope composition of pyrites from Daqiao, and other representative gold deposits in the EQO and WQO of J3–K1 and T3–J1 ages, respectively (Shi et al., 1989; Chen, 1994; Li et al., 2001, 2012b; Gong, 2014; Wu et al., 2018a).

than Co from the fluid to the solid phase during magmatic differentiation (Loftus-Hills and Solomon, 1967). Conversely, low Co/Ni ratios (<1) are thought to be typical of sedimentary pyrite (Loftus-Hills and Solomon, 1967; Large et al., 2014).

Breccia- and dyke-hosted pyrite at Daqiao have Co/Ni mean ratios of 0.36 (Wu et al., 2018a) and 0.29 (six of eight spots), respectively, and are within the range of those reported for global sedimentary pyrite (Fig. 4b; Large et al., 2014). This similarity argues against a magmatic-hydrothermal origin for the dyke-hosted pyrite, such as that inferred for pyrite from gold deposits in the EQO (Fig. 4b), and instead supports derivation of sulfur and trace metals from a sedimentary source rock. Possible candidates for such a source are the underlying Paleozoic shales and carbonaceous pelites in the WQO. These Paleozoic sediments, particularly those from the Cambrian to Silurian, have a low mean Co/Ni ratio of 0.07 (Wang, 2009).

Although Se content in dyke-hosted pyrite from DQ123 is within the range of pyrite from orogenic Au and porphyry Cu-Au deposits, pyrite from DQ477 has higher Se contents of 453 ppm (Fig. 4c; Keith et al., 2018). In marine environments, Se accumulates in organic matter due to biological uptake and substitutes for S in sedimentary pyrite (Diener and Neumann, 2011; Mitchell et al., 2012). For example, at the Bendigo orogenic gold deposit, the reported Se means are 67 ppm and 32 ppm for diagenetic and hydrothermal pyrite, respectively (Thomas et al., 2011). In the case of Se-rich hydrothermal pyrite at the Cornish, Scottish, Australian (CSA) orogenic Cu-Pb-Zn deposit, Australia, Brill (1989) proposed that Se (mean = 319 ppm) was mainly leached from the underlying sediments and transported by the metamorphic fluids. A deep-seated sedimentary Se source at Daqiao is possible, given that high Se concentrations (up to 232 ppm) are present in Paleozoic carbonaceous sediments across the QOB, such as the La'erma and Muzhuba Se (-Au) deposits in the WQO and EQO (Fig. 2; Liu and Zheng, 1993; Liu et al., 2000; Tu, 2008).

The $\delta^{34}S$ values from dyke-hosted pyrite at Daqiao exhibit a narrow range from +4.9‰ to +7.1‰ (mean + 5.6‰), suggestive of a very uniform, or well mixed, sulfur reservoir (Faure, 1986). These $\delta^{34}S$ values are similar to that of breccia ore-hosted pyrite at Daqiao (mean + 4.4‰) and of pyrite from other orogenic gold deposits of T3–J1 ages in WQO (mean + 7.5‰), which all indicate that the source of sulfur and fluids have been produced by metamorphic devolatilization of underlying Paleozoic sedimentary rocks (Fig. 5; Shi et al., 1989; Chen, 1994; Li et al., 2001; Gong, 2014; Wu et al., 2018a). In contrast, uniform and low $\delta^{34}S$ values (mean + 2.9‰) of ore stage pyrite from six gold deposits of J3–K1 ages in EQO are similar to that of magmatic pyrite from nearby pluton (2.1‰–4.3‰; Nie et al., 2001) and likely indicate a magmatic sulfur source (Li et al., 2012b).

Other similarities between the regional sediments and breccia ores at Daqiao also support sediment-derived fluids. Devonian carbonaceous phyllites and schists in the WQO are characterized by well-developed laminated diagenetic pyrite framboids that contain 0.1–1.7 ppm Au and 0.2–1.6 wt.% As (Zhang et al., 2000; Qi et al., 2003). Such Au and As enriched rocks are a possible Au and As source for the Au and As in the Daqiao ores (Wu et al., 2018a). Silurian and Cambrian siliceous rocks and carbonaceous shales that underlie Daqiao are also associated with enrichment of PGE, U, and Se (Tan, 1992; Liu and Zheng., 1993). The Daqiao breccia ores contain distinct, fine-grained hydrothermal PGE-, U- and Se-rich minerals closely associated with the ore-stage sulfides (Wu et al., 2018a).

6.3. Comparison to the EQO

The J3–K1 Daqiao gold mineralization is contemporaneous with widespread J3–K1 (ca. 150–125 Ma) magmatism and polymetallic mineralization in the EQO (Fan et al., 2011; Li et al., 2012a, b; Xie et al., 2017) and elsewhere in NE Asia (Figs. 2 and 6; Goldfarb et al., 1998, 2007; Sun et al., 2007, 2013). It has been proposed that magmatism and mineralization in the EQO is related to oblique subduction of the Paleo-Pacific ocean plate beneath the Eurasian continent (e.g., Mao et al., 2008, 2010). The plate subduction led to a regional tectonic regime transition with changes in the principal stress vectors from NS-trending at ca. 160 Ma to near EW-trending at ca. 140 Ma (Mao et al., 2005, 2006).

Structural studies of gold mines across the QOB show that T3–J1 ages deposits, such as Baguamiao, Shuangwang, Liba and

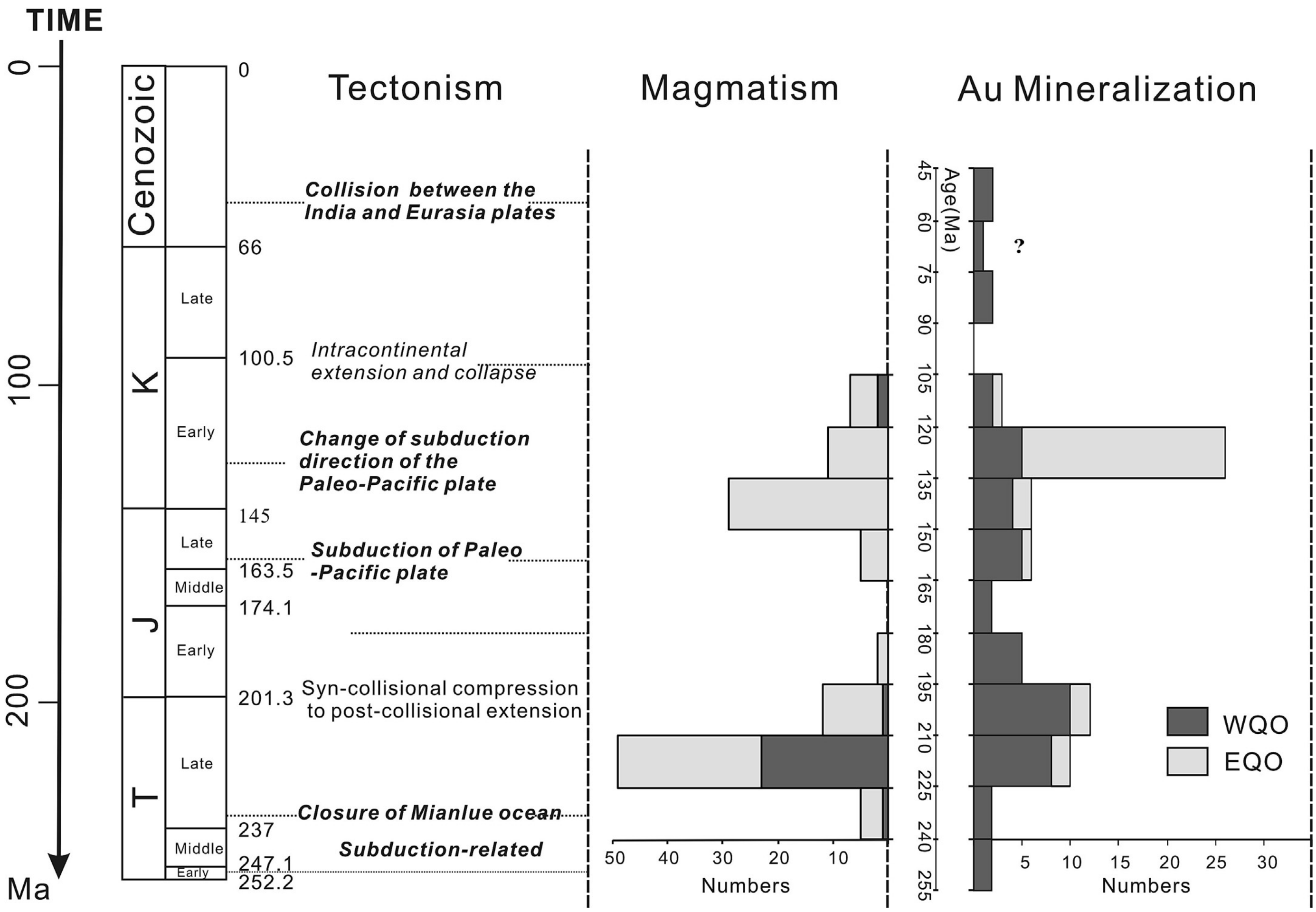

Figure 6. Summary diagram illustrating the timescales of regional tectonic events (Ren et al., 1992; Niu et al., 2003; Dong et al., 2011, 2013; Dong and Santosh, 2016), magmatism (Sun et al., 2002; Zeng et al., 2014; Xie et al., 2017), and gold mineralization (Mao et al., 2002, 2005, 2008; Chen et al., 2004; Lu et al., 2006; Qi et al., 2006; Li et al., 2012a, b; Liu et al., 2015b; Wu et al., 2018b) in the WQO and EQO.

Simaoling, are consistently controlled by WNW-trending faults and folds, whereas later NE-trending structures are barren (e.g., Gong, 2014; Wang et al., 2014; Zhang, 2016). These WNW-trending structures are thought to be a consequence of prolonged regional southward overthrusting after the T3 collision between the SCB and NCC (Chen et al., 2004). In gold deposits of J3–K1 age (e.g., Daqiao and Jinlongshan), the NE- or EW-trending brittle structures control the distribution of ore (Liu et al., 2015b; Zhang et al., 2018). In eastern China, such as the Jiaodong and Middle–Lower Yangtze belt, NE-trending faults or intersections of NE and EW-trending faults are also the dominant ore controlling structures (Fan et al., 2003; Mao et al., 2006).

In NE Asia, polymetallic mineralization peaked at ca. 150–140 Ma and 130–119 Ma and gradually decreased in intensity from east to west (Fig. 1; Li et al., 2003, 2006, 2012a, b; Mao et al., 2005). Intense mineralization mostly occurs in the circum-Pacific regions, such as Korea (granite-related Au-Ag; Choi et al., 2005), Northeast Russia (granite-related Au-Ag; Goldfarb et al., 2014), Jiaodong in East China (granite-related or orogenic Au; Qiu et al., 2002; Fan et al., 2003; Li et al., 2003, 2006), Daxing'anling in North China (granite-related Sn-Cu-Pb-Zn; Mao et al., 2005), Middle-Lower Yangtze belt in Central China (porphyry-skarn Cu-Au-Fe; Mao et al., 2006), and Nanling in South China (granite-related W-Sn-Mo-Au; Hua et al., 2005).

It is therefore interesting to consider whether subduction of the Paleo-Pacific plate influenced mineralization in the WQO, which lies about 2000 km from the current trench. On the basis of seismic data, Molnar and Tapponnier (1975) and Tapponnier and Molnar (1979) have suggested that plate collision-related continental lithosphere deformation can extend as far as 3000 km, as seen in the Eocene collision between India and Eurasia plates. If such deformation could drive sufficient heating and fluid release, then J3–K1 gold mineralization, including the Daqiao deposit, in the WQO may be, to some extent, a consequence of the tectonic regime in NE Asia, via processes related to the subduction and drifting of Paleo-Pacific plate. While it is difficult to conceptualise mechanisms that would transfer stress over such small timescales and long distances, such transfer might be facilitated by weak, young, sediments in the Qinling Orogen, that are sandwiched between the rigid, ancient, NCC and SCB.

6.4. Synthesis and implications

Most of the gold deposits, particularly in the northern belt of the WQO (e.g., Ma'anqiao, Baguamiao, Shuangwang, and Liba) were thought to form during the T3–J1 (ca. 216–203 Ma; e.g., Zeng et al., 2012; Liu et al., 2014; Wang et al., 2014; Hu, 2015; Zhang, 2016; Lin et al., 2017). Although these deposits are spatially associated with contemporaneous intrusions or dykes (ca. 220–200 Ma; Dong et al., 2011, 2013), they are thought to be related to metamorphic devolatilization of underlying Paleozoic sediments during regional deformation associated with the NCC-SCB collision and subsequent orogenic deformation (ca. 227–195 Ma; Li et al., 1996, 1999; Yang et al., 1999; Zhang et al., 2002). The entire QOB then evolved towards an intra-continental orogenic stage (Dong et al., 2011).

At ca. 140 Ma, the regional tectonic regime in the QOB changed in response to a change in plate motion (Mao et al., 2005, 2006). In the EQO, relatively intensive far-field effects triggered widespread J3–K1 magmatism and polymetallic mineralization (Mao et al., 2008, 2010; Li et al., 2012a, b; Xie et al., 2017). This intensive magmatism, which introduced fluids, sulfur and other ore components into the upper crust, was probably caused by lithospheric thinning induced by the change in Paleo-Pacific plate motion, which was accompanied by delamination and thermal erosion (Mao et al., 2010; Li et al., 2012b; Xie et al., 2017). In the WQO, no J3–K1 magmatism has been reported, which indicates a relatively low heat flow and fluid flux compared to that in EQO resulted from the lithospheric thinning (Li et al., 2012b). Geochemical evidence suggests that gold mineralization is genetically related to fluids produced by metamorphic devolatilization of underlying Paleozoic sediments. We propose that differences in the fluid sources and mineralization style of J3–K1 ages in the WQO and EQO are likely related to differences in their respective distances from the subduction front of the Paleo-Pacific plate.

To conclude, we propose that gold mineralization of J3–K1 ages in the WQO is mostly controlled by the NE- or EW-trending brittle structures and was driven to some extent by the far-effects of subduction of Paleo-Pacific plate. Better recognition and models for these structures are critical to successful exploration of J3–K1 gold deposits in the WQO.

7. Conclusion

Integration of the regional tectonics with geochronology suggests that J3–K1 gold deposits in the WQO are a consequence of far-field effects of Mesozoic subduction of the Paleo-Pacific plate beneath the Eurasian continent. J3–K1 changes in plate motion resulted in N–S trending extension and formation of NE- and EW-trending brittle structures that controlled fluid flow and gold deposition. The sources of sulfur and ore fluids in the J3–K1 age Daqiao deposit were produced by metamorphic devolatilization of the underlying Paleozoic trace element-rich sediments, which is unlike the intrusion-related deposits in the EQO. It may be that the differences in fluid source and mineralization style of J3–K1 gold deposits in the WQO and EQO are related to differences in their respective distances from the subduction front of the Paleo-Pacific plate, with important implications for the timescales and lateral extent of subduction-related effects on gold mineralization.

Acknowledgments

We acknowledge the valuable support from Daqiao Mining Ltd. and the Geological Survey of Gansu Province for access to samples and information about the Daqiao deposit. Research work was financially supported by the National Natural Science Foundation of China (Grant No. 41325007), the GPMR State Key Laboratory (grant MSFGPMR03), the China Geological Survey (Grant No. 1212011120570), and National Demonstration Center for Experimental Mineral Exploration Education at China University of Geosciences (Wuhan). The senior author acknowledges the receipt of a Chinese Scholarship Council/Curtin International Postgraduate Research Scholarship. This paper benefited from constructive reviews from Albert H Hofstra and other three anonymous reviewers. Ours thanks go to editorial suggestions from Handling Editor Dr. Christopher Spencer.

References

Belousov, I., Large, R.R., Meffre, S., Danyushevsky, L.V., Steadman, J., Beardsmore, T., 2016. Pyrite compositions from VHMS and orogenic Au deposits in the Yilgarn Craton, Western Australia: implications for gold and copper exploration. Ore Geology Reviews 79, 474–499.

Bi, S.J., Li, Z.K., Tang, K.F., Gao, K., 2016. LA-ICP-MS in situ trace element analysis of pyrite from Dongtongyu gold deposit and its metallogenic significance. Earth Science 41, 1121–1140 (in Chinese with English abstract).

Brill, B.A., 1989. Trace-element contents and partitioning of elements in ore minerals from the CSA Cu-Pb-Zn deposit, Australia, and implications for ore genesis. The Canadian Mineralogist 27, 263–274.

Chen, Y., 1994. Sources of ore-forming materials in the Liba gold deposit, west Qinling orogen. Northwestern Geology 15, 5–9 (in Chinese with English abstract).

Chen, Y.J., Zhang, J., Zhang, F.X., Franco, P., Li, C., 2004. Carlin and Carlin-like gold deposits in the Western Qinling Mountains and their metallogenic time, tectonic setting and model. Geological Review 50, 134–152 (in Chinese with English abstract).

Choi, S.G., Kwon, S.T., Ree, J.H., So, C.S., Pak, S.J., 2005. Origin of Mesozoic gold mineralization in South Korea. The Island Arc 14, 102–114.

Diener, A., Neumann, T., 2011. Synthesis and incorporation of selenide in pyrite and mackinawite. Radiochimica Acta 99, 791–798.

Dong, Y.P., Zhang, G.W., Neubauer, F., Liu, X.M., Genser, J., Hauzenberger, C., 2011. Tectonic evolution of the Qinling orogen, China: review and synthesis. Journal of Asian Earth Sciences 41, 213–237.

Dong, Y.P., Liu, X.M., Neubauer, F., Zhang, G.W., Tao, N., Zhang, Y.G., Zhang, X.N., Li, W., 2013. Timing of paleozoic amalgamation between the north China and south China blocks: evidence from detrital zircon U-Pb ages. Tectonophysics 586, 173–191.

Dong, Y.P., Santosh, M., 2016. Tectonic architecture and multiple orogeny of the Qinling orogenic belt, central China. Gondwana Research 29, 1–40.

Fan, H.R., Zhai, M.G., Xie, Y.H., Yang, J.H., 2003. Ore-forming fluids associated with granite-hosted gold mineralization at the Sanshandao deposit, Jiaodong gold province, China. Mineralium Deposita 38, 739–750.

Fan, H.R., Hu, F.F., Wilde, S.A., Yang, K.F., Jin, C.W., 2011. The Qiyugou gold-bearing breccia pipes, Xiong'ershan region, central China: fluid inclusion and stable-isotope evidence for an origin from magmatic fluids. International Geology Review 53, 25–45.

Faure, G., 1986. Principles of Isotope Geology, second ed. John Wiley and Sons, New York, p. 1779.

Genna, D., Gaboury, D., 2015. Deciphering the hydrothermal evolution of a VMS system by LA-ICP-MS using trace elements in pyrite: an example from the Bracemac-McLeod deposits, Abitibi, Canada, and implications for exploration. Economic Geology 110, 2087–2108.

Gilbert, S.E., Danyushevsky, L.V., Rodemann, T., Shimizu, N., Gurenko, A., Meffre, S., Thomas, H., Large, R.R., Death, D., 2014. Optimisation of laser parameters for the analysis of sulphur isotopes in sulphide minerals by laser ablation ICP-MS. Journal of Analytical Atomic Spectrometry 29, 1042–1051.

Goldfarb, R.J., Phillips, G.N., Nokleberg, W.J., 1998. Tectonic setting of synorogenic gold deposits of the Pacific Rim. Ore Geology Reviews 13, 185–218.

Goldfarb, R.J., Hart, C., Davis, G., Groves, D., 2007. East Asian gold: deciphering the anomaly of Phanerozoic gold in precambrian cratons. Economic Geology 102, 341–345.

Goldfarb, R.J., Taylor, R.D., Collins, G.S., Goryachev, N.A., Orlandini, O.F., 2014. Phanerozoic continental growth and gold metallogeny of Asia. Gondwana Research 25, 48–102.

Gong, Y.J., 2014. The Study on the Tectonic-fluid System and Metallogeni Mechanism of Shuangwang Gold Deposit in Shaanxi Province. Ph.D. thesis. China University of Geosciences, Wuhan, p. 101p (in Chinese with English abstract).

Hu, Q.Q., 2015. The Mineralization Features, Mechanism and Metallogenic Regularity of the Fengtai Pb-zn Polymetallic Ore Cluster in West Qinling, China. Ph.D. thesis. Chinese Academy of Geological Sciences, p. 150 (in Chinese with English abstract).

Hua, R.M., Chen, P.R., Zhang, W.L., Yao, J.M., Lin, J.F., Zhang, Z.S., Gu, S.Y., Liu, X.D., Qi, H.W., 2005. Metallogenesis related to Mesozoic granitoids in the Nanling Range, South China and their geodynamic settings. Acta Geologica Sinica 79, 810–820 (in Chinese with English abstract).

Huang, W.K., Gan, X.P., Shan, Z.X., Chen, L.X., Liu, Y., 1996. A study of petrology and metallognetic epoch of gold in Jianchaling deposit, Shaanxi Province. Geochimica 25, 150–156 (in Chinese with English abstract).

Huston, D.L., Sie, S.H., Suter, G.F., Cooke, D.R., Both, R.A., 1995. Trace elements in sulfide minerals from eastern Australian volcanic-hosted massive sulfide deposits; Part I, Proton microprobe analyses of pyrite, chalcopyrite, and sphalerite, and Part II, Selenium levels in pyrite; comparison with delta ^{34}S values and implications for the source of sulfur in volcanogenic hydrothermal systems. Economic Geology 90, 1167–1196.

Keith, M., Smith, D.J., Jenkin, G.R., Holwell, D.A., Dye, M.D., 2018. A review of Te and Se systematics in hydrothermal pyrite from precious metal deposits: insights into ore-forming processes. Ore Geology Reviews 96, 269–282.

Koppers, A.A.P., Staudigel, H., Duncan, R.A., 2003. High-resolution $^{40}Ar/^{39}Ar$ dating of the oldest oceanic basement basalts in the western Pacific basin. Geochemistry, Geophysics, Geosystems 4, 8914.

Lan, T.G., Fan, H.R., Santosh, M., Hu, F.F., Yang, K.F., Yang, Y.H., Liu, Y., 2011. Geochemistry and Sr-Nd-Pb-Hf isotopes of the Mesozoic Dadian alkaline intrusive complex in the Sulu orogenic belt, eastern China: implications for crust–mantle interaction. Chemical Geology 285, 97–114.

Large, R.R., Danyushevsky, L., Hollit, C., Maslennikov, V., Meffre, S., Gilbert, S., Bull, S., Scott, R., Embsbo, P., Thomas, H., Singh, B., Foster, J., 2009. Gold and trace element zonation in pyrite using a laser imaging technique: implications for the timing of gold in orogenic and Carlin style sediment-hosted deposits. Economic Geology 104, 635–668.

Large, R.R., Halpin, J.A., Danyushevsky, L.V., Maslennikov, V.V., Bull, S.W., Long, J.A., Gregory, D.D., Lounejeva, E., Lyons, T.W., Sack, P.J., McGoldrick, P.J., Calve, C.R., 2014. Trace element content of sedimentary pyrite as a new proxy for deep-time ocean-atmosphere evolution. Earth and Planetary Science Letters 389, 209–220.

Li, F.D., Zou, X.H., Gao, J.P., Lu, Y., Zhang, H.Y., 2001. On the rapid-positioning and prediction for micro dissemination type (sedimentary rock host) gold deposit (ore bodies), Ma'anqiao. Northwestern Geology 34, 27–63 (in Chinese with English abstract).

Li, J.W., Vasconcelos, P.M., Zhang, J., Zhou, M.F., Zhang, X.J., Yang, F.H., 2003. $^{40}Ar/^{39}Ar$ constraints on a temporal link between gold mineralization, magmatism, and continental margin transtension in the Jiaodong gold province, eastern China. The Journal of Geology 111, 741–751.

Li, J.W., Vasconcelos, P.M., Zhou, M.F., Zhao, X.F., Ma, C.Q., 2006. Geochronology of the Pengjiakuang and Rushan gold deposits, eastern Jiaodong gold province, northeastern China: implications for regional mineralization and geodynamic setting. Economic Geology 101, 1023–1038.

Li, J.W., Li, Z.K., Zhou, M.F., Chen, L., Bi, S.J., Deng, X.D., Qiu, H.N., Cohen, B., Zhao, X.F., 2012a. The Early Cretaceous Yangzhaiyu lode gold deposit, North China Craton: a link between craton reactivation and gold veining. Economic Geology 107, 43–79.

Li, J.W., Bi, S.J., Selby, D., Chen, L., Vasconcelos, P., Thiede, D., Zhou, M.F., Zhao, X.F., Li, Z.K., Qiu, H.N., 2012b. Giant Mesozoic gold provinces related to the destruction of the North China craton. Earth and Planetary Science Letters 349, 26–37.

Li, J.Y., Wang, Z.Q., Zhao, M., 1999. $^{40}Ar/^{39}Ar$ thermochronological constraints on the timing of collisional orogeny in the Mian-Lue collision belt, southern Qinling Mountains. Acta Geologica Sinica 73, 208–215 (in Chinese with English abstract).

Li, S.G., Sun, W.D., Zhang, G.W., 1996. Chronology and geochemistry of metavolcanic rocks from Heigouxia valley in Mian-Lue tectonic belt, South Qinling: evidence for a Paleozoic oceanic basin and its close time. Science in China (Series D) 39, 300–310.

Lin, Z.W., Zhou, Y.Z., Qin, Y., Yue, S.W., 2017. Fuchsite $^{40}Ar/^{39}Ar$ geochronology of the Huachanggou gold Deposit and its tectonic implications. Geotectonica et Metallogenia 41, 315–327 (in Chinese with English abstract).

Liu, J.J., Zheng, M.H., 1993. La'erma Se-Cu-U-Ni-Mo-PGE-Au deposit of submarine exhalative genesis in La'erma. Journal of Precious Metallic Geology 2, 100–103 (in Chinese with English abstract).

Liu, J.J., Zheng, M.H., Liu, J.M., Su, W.C., 2000. Geochemistry of the La'erma and Qiongmo Au-Se deposits in the western Qinling mountains, China. Ore Geology Reviews 17, 91–111.

Liu, J.J., Dai, H.Z., Zhai, D.G., Wang, J.P., Wang, Y.H., Yang, L.B., Mao, G.J., Liu, X.H., Liao, Y.F., Yu, C., Li, Q.Z., 2015a. Geological and geochemical characteristics and formation mechanisms of the Zhaishang Carlin-like type gold deposit, western Qinling Mountains, China. Ore Geology Reviews 64, 273–298.

Liu, X.L., Wang, Y.T., Hu, Q.Q., Wei, R., Wang, R.T., Wen, S.W., Chen, M.S., Yang, G.H., 2014. Sm-Nd isotopic dating of carbonate minerals from the Chaima gold deposit in the Fengxian-Taibai ore concentration area, Shaanxi Province and its implications. Acta Petrologica Sinica 30, 271–280 (in Chinese with English abstract).

Liu, Y.H., Li, Z., Zhou, S., Han, Y.X., Li, H., Li, X., Zhou, S.F., 2015b. Geological characteristics, ore-forming ages and geological significance of Donggou-Jinlongshan gold deposit, South Qinling belt. Earth Science Frontiers 22, 1–13 (in Chinese with English abstract).

Loftus-Hills, G., Solomon, M., 1967. Cobalt, nickel and selenium in sulphides as indicators of ore genesis. Mineralium Deposita 2, 228–242.

Longerich, H.P., Jackson, S.E., Günther, D., 1996. Laser ablation inductively coupled plasma mass spectrometric transient signal data acqusition and analyte concentration calculation. Journal of Analytical Atomic Spectroscopy 11, 899–904.

Lu, Y.M., Li, H.G., Chen, Y.G., Zhang, G.L., 2006. $^{40}Ar/^{39}Ar$ dating of alteration minerals from Zhaishang gold deposit in Minxian County, Gansu Province, and its geologic significance. Mineral Deposits 25, 590–597 (in Chinese with English abstract).

Meng, Q.R., Zhang, G.W., 1999. Timing of collision of the north and south China blocks: controversy and reconciliation. Geology 27, 123–126.

Mao, J.W., Qiu, Y.M., Goldfarb, R.J., Zhang, Z.C., Garwin, S., Fengshou, R., 2002. Geology, distribution, and classification of gold deposits in the western Qinling belt, central China. Mineralium Deposita 37, 352–377.

Mao, J.W., Xie, G.Q., Zhang, Z.H., Li, X.F., Wang, Y.T., Zhang, C.Q., Li, Y.F., 2005. Mesozoic large-scale metallogenic pulses in North China and corresponding geodynamic settings. Acta Petrologica Sinca 21, 169–188 (in Chinese with English abstract).

Mao, J.W., Wang, Y.T., Lehmann, B., Yu, J.J., Du, A.D., Mei, Y.X., Li, Y.F., Zang, W.S., Stein, H.J., Zhou, T.F., 2006. Molybdenite Re-Os and albite $^{40}Ar/^{39}Ar$ dating of Cu-Au-Mo and magnetite porphyry systems in the Yangtze River valley and metallogenic implications. Ore Geology Reviews 29, 307–324.

Mao, J.W., Xie, G.Q., Bierlein, F., Qu, W.J., Du, A.D., Ye, H.S., Pirajno, F., Li, H.M., Guo, B.J., Li, Y.F., Yang, Z.Q., 2008. Tectonic implications from Re-Os dating of Mesozoic molybdenum deposits in the East Qinling-Dabie orogenic belt. Geochimica et Cosmochimica Acta 72, 4607–4626.

Mao, J.W., Xie, G.Q., Pirajno, F., Ye, H.S., Wang, Y.B., Li, Y.F., Xiang, J.F., Zhao, H.J., 2010. Late Jurassic-Early Cretaceous granitoid magmatism in Eastern Qinling, central-eastern China: SHRIMP zircon U-Pb ages and tectonic implications. Australian Journal of Earth Sciences 57, 51–78.

Mitchell, K., Mason, P.R., Van Cappellen, P., Johnson, T.M., Gill, B.C., Owens, J.D., Diaz, J., Ingall, E.D., Reichart, G.J., Lyons, T.W., 2012. Selenium as paleo-oceanographic proxy: a first assessment. Geochimica et Cosmochimica Acta 89, 302–317.

Molnar, P., Tapponnier, P., 1975. Cenozoic tectonics of Asia: effects of a continental collision. Science 189, 419–426.

Müller, W., Shelley, M., Miller, P., Broudec, S., 2009. Initial performance metrics of a new custom-designed ArF excimer LA-ICPMS system coupled to a two-volume laser-ablation cell. Journal of Analytical Atomic Spectrometry 24, 209–214.

Nie, F.J., Jiang, S.H., Zhao, Y.M., 2001. Lead and sulfur isotope study of the Wenyu and Dongchuang quartz vein-type gold deposits in the Xiaoqinling area, Henan and Shaanxi Province, central China. Mineral Deposita 20, 163–173 (in Chinese with English abstract).

Niu, B.G., He, Z.J., Song, B., Ren, J.S., 2003. SHRIMP dating of the Zhangjiakou volcanic series and its significance. Geological Bulletin of China 22, 140–141 (in Chinese with English abstract).

Price, B.J., 1972. Minor Elements in Pyrites from the Smithers Map Area, British Columbia and Exploration Applications of Minor Element Studies. M.S. thesis. The University of British Columbia, p. 270.

Qi, J.Z., Yuan, S.S., Li, L., Sun, B., Guo, J.H., Li, Z.H., Fan, Y.X., Liu, W., Gao, Q.B., 2003. Geological features and ore-controlling factors of the Yangshan superlarge gold deposit, Gansu province, China. Geological Review 49, 85–92 (in Chinese with English abstract).

Qi, J.Z., Yang, G.C., Li, L., Fan, Y.X., Liu, W., 2006. Isotope geochemistry, chronology and genesis of the Yangshan gold deposit, Gansu. Geology in China 33, 1345–1353 (in Chinese with English abstract).

Qiu, Y.M., Groves, D.I., McNaughton, N.J., Wang, L.G., Zhou, T.H., 2002. Nature, age, and tectonic setting of granitoid-hosted, orogenic gold deposits of the Jiaodong Peninsula, eastern North China craton, China. Mineralium Deposita 37, 283–305.

Ratschbacher, L., Hacker, B.R., Calvert, A., Webb, L.E., Grimmer, J.C., McWilliams, M.O., Hu, J., 2003. Tectonics of the Qinling (Central China): tectonostratigraphy, geochronology, and deformation history. Tectonophysics 366, 1–53.

Ren, J.S., Chen, T.Y., Niu, B.G., 1992. Tectonic Evolution of the Continental Lithosphere of the East China and Adjacent Area and Relevant Mineralization. Science Press, Beijing, p. 230 (in Chinese).

Shan, L., Zhang, D.M., Pang, Y.C., Liu, J.J., Zhang, W.Y., Zhao, M.M., Zhang, Z.P., 2016. Late Triassic magmatic activity in the Daqiao gold deposit of West Qinling belt: zircon U-Pb chronology and Lu-Hf isotope evidence. Geological Bulletin of China 35, 2045–2057 (in Chinese with English abstract).

Shi, Z.L., Liu, J.X., Fan, S.C., 1989. Geological Characteristics and Genesis of Shuangwang Gold Deposit, Shaanxi Province. Science and Technology Publishing House of Shaanxi, Xi'an, p. 98.

Sun, W.D., Li, S.G., Chen, Y.D., Li, Y.J., 2002. Timing of synorogenic granitoids in the South Qinling, central China: constraints on the evolution of the Qinling-Dabie orogenic belt. The Journal of Geology 110, 457–468.

Sun, W.D., Ding, X., Hu, Y.H., Li, X.H., 2007. The golden transformation of the Cretaceous plate subduction in the west Pacific. Earth and Planetary Science Letters 262, 533–542.

Sun, W.D., Ling, M.X., Yang, X.Y., Fan, W.M., Ding, X., Liang, H.Y., 2010. Ridge subduction and porphyry copper-gold mineralization: an overview. Science China Earth Sciences 53, 475–484.

Sun, W.D., Li, S., Yang, X.Y., Ling, M.X., Ding, X., Duan, L.A., Zhan, M.Z., Zhang, H., Fan, W.M., 2013. Large-scale gold mineralization in eastern China induced by an Early Cretaceous clockwise change in Pacific plate motions. International Geology Review 55, 311–321.

Tan, G.Y., 1992. Geological character of Pingding As-Au deposit and its metallogenic mechanism. Acta Geologica Gansu 1, 48–54 (in Chinese with English abstract).

Tapponnier, P., Molnar, P., 1979. Active faulting and cenozoic tectonics of the tien Shan, Mongolia, and Baykal regions. Journal of Geophysical Research Solid Earth 84, 3425–3459.

Thomas, H.V., Large, R.E., Bull, S.W., Maslennikov, V., Berry, R.F., Fraser, R., Froud, S., Moye, R., 2011. Pyrite and pyrrhotite textures and composition in sediments, laminated quartz veins, and reefs at Bendigo gold mine, Australia: insights for ore genesis. Economic Geology 106, 1–31.

Tu, H.K., 2008. Discovery and application of the Qinling Se deposit with its forming mechanism research. Mineral Resources and Geology 22, 27–32 (in Chinese with English abstract).

Wang, L.S., 2009. Study on the metallogenic regularity and geological-geochemistry for black rock series and related typical deposits. Ph.D. thesis. In: Qinling Mountains, Shaanxi. Northwest University, p. 165 (in Chinese with English abstract).

Wang, Y.T., Li, X., Wang, R.T., Liu, X.L., Hu, Q.Q., Li, J.H., 2014. Evidence of Ar-Ar age for the metallogenic epoch of Simaoling gold deposit in Fengxian-Taibai ore cluster of Shaanxi. Journal of Earth Science and Environment 36, 61–72 (in Chinese with English abstract).

Wilson, S.A., Ridley, W.I., Koenig, A.E., 2002. Development of sulfide calibration standards for the laser ablation inductively coupled plasma mass spectrometry technique. Journal of Analytical Atomic Spectroscopy 17, 406–409.

Wong, K.H., Zhou, M.F., Chen, W.T., O'Brien, H., Lahaye, Y., Chan, S.L.J., 2017. Constraints of fluid inclusions and in-situ S-Pb isotopic compositions on the origin of the North Kostobe sediment-hosted gold deposit, eastern Kazakhstan. Ore Geology Reviews 81, 256–269.

Wu, F.F., Wang, Z.Q., Yan, Z., Chen, L., Xia, C.L., Guo, Y.H., Peng, Y.M., 2014. Geochemical characteristics, zircons U-Pb ages and Lu-Hf isotopic composition of the Yanshanian intermediate-acidic plutons in the Shanyang-Zhashui areas, Qinling Orogenic Belt. Acta Petrologica Sinica 30, 451–471 (in Chinese with English abstract).

Wu, Y.F., Li, J.W., Evans, K., Koenig, A.E., Li, Z.K., O'Brien, H., Lahaye, Y., Rempel, K., Hu, S.Y., Zhang, Z.P., Yu, J.P., 2018a. Ore-forming processes of the Daqiao Epizonal orogenic gold deposit, West Qinling orogen, China: constraints from textures, trace elements, and sulfur isotopes of pyrite and marcasite, and Raman spectroscopy of carbonaceous material. Economic Geology 113, 1093–1132.

Wu, Y.F., Li, J.W., Evans, K., Vasconcelos, P.M., Thiede, D.S., Fougerouse, D., Rempel, K., 2018b. Late Jurassic to early cretaceous age of the Daqiao gold deposit, West Qinling orogen, China: implications for regional metallogeny. Mineralium Deposita 53. https://doi.org/10.1007/s00126-018-0835-z.

Xie, G.Q., Mao, J.W., Wang, R.T., Meng, D.M., Sun, J., Dai, J.Z., Ren, T., Li, J.B., Zhao, H.J., 2017. Origin of the Lengshuigou porphyry-skarn Cu deposit in the Zha-Shan district, South Qinling, central China, and implications for differences between porphyry Cu and Mo deposits. Mineralium Deposita 52, 621–639.

Yang, C.H., Wei, C.J., Zhang, S.G., Li, H.M., Wan, Y.S., Li, R.S., 1999. U-Pb zircon dating of granulite facies rocks from the Foping area in the southern Qinling mountains. Geological Review 45, 173–179.

Zeng, Q.T., McCuaig, T.C., Hart, C.J.R., Jourdan, F., Muhling, J., Bagas, L., 2012. Structural and geochronological studies on the Liba goldfield of the West Qinling orogen, Central China. Mineralium Deposita 47, 799–819.

Zeng, Q.T., Mccuaig, T.C., Tohver, E., Bagas, L., Lu, Y.J., 2014. Episodic Triassic magmatism in the western South Qinling orogen, central China, and its implications. Geological Journal 49, 402–423.

Zhai, Y., Deng, J., 1996. Outline of the mineral resources of China and their tectonic setting. Australian Journal of Earth Sciences 43, 673–685.

Zhang, F.X., Chen, Y.J., Li, C., Zhang, J., Ma, J.Q., Li, X., 2000. Features of geologic-geochemistry of Jinlongshan-Qiuling gold deposit and its genesis in Qinling belt: dynamics on mineralizing process of Carlin type gold deposits of Qinling type. Science in China Series D Earth Sciences 30 (Suppl. I), 73–81 (in Chinese with English abstract).

Zhang, G.W., Zhang, Z.Q., Dong, Y.P., 1995. Nature of main tectono-lithostratigraphic units of the Qinling Orogen: implications for the tectonic evolution. Acta Petrologica Sinica 11, 101–114 (in Chinese with English abstract).

Zhang, G.W., Zhang, B.R., Yuan, X.C., Xiao, Q.H., 2001. Qinling Orogenic Belt and Continental Dynamics. Science Press, Beijing, p. 855 (in Chinese).

Zhang, J., 2016. Study of Mineralization Process and Mechanism in Baguamiao Super Large Gold Deposit, Fengtai Ore Region, Shaanxi, China. Ph.D. thesis. Chinese Academy of Geological Sciences, p. 200 (in Chinese with English abstract).

Zhang, J., Li, L., Gilbert, S., Liu, J.J., Shi, W.S., 2014. LA-ICP-MS and EPMA studies on the Fe-S-As minerals from the Jinlongshan gold deposit, Qinling Orogen, China: implications for ore-forming processes. Geological Journal 49, 482–500.

Zhang, Z.P., Wu, Y.F., Li, J.W., 2018. Characteristics and genesis of the silicified breccias in the Daqiao gold deposit, West Qinling Orogen. Geological Science and Technology Information 37, 79–88.

Zhang, Z.Q., Zhang, G.W., Tang, S.H., Wang, J.H., Xu, J.F., Yang, Y.C., 2002. Age of Anzishan granulites in the Mianxian-Lueyang suture zone of Qinling orogen: with a discussion of the timing of final assembly of Yangtze and north China craton blocks. Chinese Science Bulletin 47, 1925–1929.